Strong effect of scandium source purity on chemical and electronic properties of epitaxial $Sc_xAl_{1-x}N$/GaN heterostructures

Cite as: APL Mater. 9, 091106 (2021); doi: 10.1063/5.0054522
Submitted: 19 April 2021 • Accepted: 15 August 2021 •
Published Online: 7 September 2021

Joseph Casamento,[1,a] Hyunjea Lee,[2] Celesta S. Chang,[3,4,b] Matthew F. Besser,[5] Takuya Maeda,[6] David A. Muller,[3,6] Huili (Grace) Xing,[1,2,6] and Debdeep Jena[1,2,6]

AFFILIATIONS

[1] Department of Materials Science and Engineering, Cornell University, Ithaca, New York 14853, USA
[2] School of Electrical and Computer Engineering, Cornell University, Ithaca, New York 14853, USA
[3] Department of Physics, Cornell University, Ithaca, New York 14853, USA
[4] School of Applied and Engineering Physics, Cornell University, Ithaca, New York 14853, USA
[5] Division of Materials Sciences and Engineering, Ames Laboratory, Ames, Iowa 50011, USA
[6] Kavli Institute at Cornell for Nanoscale Science, Cornell University, Ithaca, New York 14853, USA

[a] **Author to whom correspondence should be addressed:** jac694@cornell.edu
[b] **Present address:** Research Laboratory of Electronics, Massachusetts Institute of Technology, Cambridge, Massachusetts 02139, USA.

ABSTRACT

Epitaxial multilayer heterostructures of $Sc_xAl_{1-x}N$/GaN with Sc contents x = 0.11–0.45 are found to exhibit significant differences in structural quality, chemical impurity levels, and electronic properties depending on the starting Sc source impurity levels. A higher purity source leads to a 2–3 orders of magnitude reduction in the carbon, oxygen, and fluorine unintentional doping densities in MBE-grown $Sc_xAl_{1-x}N$/GaN multilayers. Electrical measurements of $Sc_xAl_{1-x}N/n^+$GaN single heterostructure barriers show a 5–7 orders of magnitude reduction in the electrical leakage for films grown with a higher purity Sc source at most Sc contents. The measured chemical and electrical properties of epitaxial $Sc_xAl_{1-x}N$ highlight the importance of the starting Sc source material purity for epitaxial device applications that need these highly piezoelectric and/or ferroelectric transition-metal nitride alloys.

Alloying of aluminum nitride (AlN) with the transition element scandium (Sc) has garnered significant research interest due to a significant increase in the piezoelectric and pyroelectric response, and even ferroelectric behavior.[1–7] This is due to the unique predicted ability of Sc and other early transition metal atoms (e.g., yttrium) to have a large solubility in the wurtzite crystal structure, in addition to isoelectronic alloying from a natural +3 oxidation state.[8–11] Combined with the merit Al(Ga)N layers already found in numerous applications in photonic devices, such as LEDs and lasers, solid-state lighting, telecommunications, piezoelectric devices, and high power and high frequency electronics,[12–16] $Sc_xAl_{1-x}N$ is a rapidly emerging technologically relevant material.

Epitaxial growth of highly crystalline $Sc_xAl_{1-x}N$ thin films presents several challenges stemming from the fundamental mismatch in the stable crystal structures of the components: ScN adopts a rock salt crystal structure, whereas AlN is wurtzite. Rock salt ScN is non-piezoelectric and non-pyroelectric, whereas AlN boasts both piezoelectric and spontaneous polarization. Wurtzite ScN is a metastable phase that has never been realized experimentally.[17–19] Accordingly, thermodynamic phase separation in $Sc_xAl_{1-x}N$ is predicted beyond a certain atomic percentage of Sc: kinetic factors during deposition can potentially reduce this transition threshold. Any phase separation into cubic ScN or cubic Sc-rich $Sc_{1-x}Al_xN$ regions is expected to be deleterious to piezoelectric and ferroelectric properties. Additionally, Sc has a large thermodynamic driving force to bond with oxygen.[20,21] This is fundamentally due to the large electronegativity difference between Sc and oxygen, the small effective nuclear charge of Sc 3*d* orbitals, and the high energy

of the Sc 3*d* orbitals.[22–24] These all contribute to a large negative Gibbs free energy in the formation of the Sc–O bond relative to metallic Sc. When combined, these challenges manifest themselves in the form of chemical inhomogeneities, excess impurity incorporation, and microstructural instabilities in as-grown $Sc_xAl_{1-x}N$ films.[25–33] As $Sc_xAl_{1-x}N$ gains interest for applications in epitaxial heterostructures for photonics and electronics,[34–49] where performance is extremely sensitive to impurity concentrations and chemical doping, these issues need to be addressed at this time since studies of the epitaxial material are at an early stage.

As $Sc_xAl_{1-x}N$ increases in technological relevance, the purification of Sc is starting to acquire increased relevance. Sc, along with other rare earth metals, is difficult to purify, in part due to the chemical trends mentioned above. This results in commercially available Sc sources being of lower purity than other metals used in the III-nitride family (e.g., Ga, In, and Al, which can be purified to 6–7N purity levels in their elemental form). Fortunately, effort has been dedicated to the improvement of Sc metal purity. Notably, a process has been developed at the Ames Laboratory, which uses anhydrous fluorination to convert Sc_2O_3 to ScF_3, which is subsequently converted to relatively pure Sc by calcium reduction.[50] This process does not represent the fundamental limits of Sc purification, as additional steps such as electrotransport[51] can be utilized to purify Sc even further.

In this work, we report the differences in the structural and chemical properties of epitaxial, single-crystalline $Sc_xAl_{1-x}N$/GaN multilayer heterostructures, where the Sc content is varied between x = 0.11 and 0.45 mole fraction, when grown with two Sc sources of different chemical purity levels. The multilayer heterostructures have 120 nm thick periods and are grown by plasma-assisted MBE on semi-insulating GaN/Al_2O_3 template substrates. GaN/Al_2O_3 template substrates were chosen due to their commercial availability, insulating nature, and in-plane lattice matching to $Sc_xAl_{1-x}N$ at ~18% Sc (x = 0.18). Combined, this heterostructure is well suited to study the chemical behavior of $Sc_xAl_{1-x}N$ and epitaxially stabilize wurtzite $Sc_xAl_{1-x}N$. *In situ* reflection high-energy electron diffraction (RHEED) images of $Sc_xAl_{1-x}N$ indicate epitaxial growth for all layers and suggest that GaN maintains a wurtzite crystal structure when grown on top of $Sc_xAl_{1-x}N$ at all Sc compositions studied. Secondary ion mass spectrometry (SIMS) measurements, calibrated by Rutherford backscattering spectrometry (RBS) data, are then used to uncover a 2–3 orders of magnitude reduction in the carbon, oxygen, and fluorine impurity levels in the film grown with a higher purity Sc source. High-angle annular dark field scanning transmission electron microscopy (HAADF-STEM) images corroborate the RHEED indications. Separate $Sc_xAl_{1-x}N$ films of ~100 nm thickness grown on n^+GaN bulk substrates were then used to assess electrical conductivity. $Sc_xAl_{1-x}N$ films grown with the higher purity Sc source demonstrated 5–7 orders of magnitude reduction in the leakage current density. Lowering leakage is critical for accessing high voltages in RF transistors, and large coercive fields are needed to study ferroelectric and enhanced piezoelectric behavior.

The $Sc_xAl_{1-x}N$/GaN heterostructures of this work were grown by MBE in a Veeco® GenXplor system with a base pressure of 10^{-10} Torr on Xiamen® 10 × 10 mm^2 semi-insulating GaN/Al_2O_3 substrates for SIMS measurements, and separately on Suzhou Nanowin® 7 × 7 mm^2 conductive *n*-type bulk GaN substrates for electrical measurements. Two Sc metal sources, one of nominally 99.9% purity (including C and O impurities) from Ames Laboratory and another of 99.99% purity (on a rare earth element basis) from a commercial vendor, were used for the comparative study. They were evaporated from separate W crucibles using a Telemark® electron beam evaporation system integrated with the MBE equipment. Flux feedback was achieved with an Inficon® electron impact emission spectroscopy (EIES) system by directly measuring the Sc atomic optical emission spectra. Aluminum (99.9999% purity), gallium (99.999 99% purity), and silicon (99.9999% purity) were supplied using Knudsen effusion cells. Nitrogen (99.999 95%) active species were supplied using a Veeco RF UNI-Bulb plasma source, with a growth pressure of ~10^{-5} Torr. The reported growth temperature is the substrate heater temperature measured by a thermocouple. *In situ* monitoring of film growth was performed using a KSA Instruments reflection high energy electron diffraction (RHEED) apparatus with a Staib electron gun operating at 15 kV and 1.5 A. Post-growth X-Ray Diffraction (XRD) was performed on a Panalytical Empyrean® diffractometer at 45 kV, 40 mA with Cu Kα1 radiation (1.540 57 Å). Post growth AFM measurements were performed using an Asylum Research Cypher ES system. Cross-sectional STEM samples were prepared via the focused ion beam (FIB) lift-out method using a Thermo Fisher Helios G4 UX FIB. Protective layers of carbon, Pt, and AuPd were sputtered prior to the FIB to prevent surface damage. High-angle annular dark field scanning transmission electron microscopy (HAADF-STEM) was performed using a convergence angle of 21 mrad in an aberration-corrected FEI Themis Titan microscope operating at 300 keV. SIMS and RBS measurements were performed at Evans Analytical Group (EAG). An AlN reference sample was utilized as ion implant standards do not currently exist for $Sc_xAl_{1-x}N$. Quasi-static electrical current–voltage (I–V) measurements were performed on a Cascade Microtech 11000 probe station in an N_2 ambient condition at room temperature on 40 μm diameter circular Ti/Au electrodes patterned lithographically on separate $Sc_xAl_{1-x}N$/GaN heterostructure samples.

All $Sc_xAl_{1-x}N$/GaN heterostructures for this study were epitaxially grown in a reactive nitrogen environment in the MBE chamber at 200 W RF nitrogen plasma power and 1.95 SCCM flow rate. Sc and Al atomic percentages in the film were adjusted by the ratio of the respective fluxes from the effusion cell for Al and E-Beam for Sc. The beam equivalent pressures (BEPs) measured from a beam flux monitor (BFM) right below the substrate surface ranged from F_{Al} = 1.3 × 10^{-7} to 2 × 10^{-7} Torr for Al and F_{Sc} = 3.0 × 10^{-8} to 1 × 10^{-7} Torr for Sc. The $Sc_xAl_{1-x}N$ layers were grown under nitrogen rich conditions with III/V ratio ~0.85 at a substrate temperature of ~600 °C, with a growth rate of ~6 nm/min. Sc and Al were co deposited continuously during the growth. These conditions were utilized to prevent excess metal accumulation on the surface, which in turn prevents the formation of undesired yet thermodynamically favorable Sc–Al containing intermetallic compounds that form in metal-rich growth conditions. A more detailed study of the growth conditions and calibration of the active nitrogen flux used to establish the effective III/V ratio is described elsewhere.[52] It is noted that there are several growth methods and characterizations that can be used to calibrate the active nitrogen flux (N^*), and accordingly, the III/V ratio. The GaN layers were grown under metal rich conditions with III/V ratio >1 at 700 °C substrate temperature to promote smooth surfaces. Any excess Ga was consumed by keeping the nitrogen plasma shutter open and monitoring the RHEED specular intensity. This

TABLE I. Summary of Sc contents measured by RBS on the two $Sc_xAl_{1-x}N$-GaN heterostructures further analyzed via XRD and SIMS, and STEM in this report.

Sc atomic percentages with lower purity Sc source	Sc atomic percentages with higher purity Sc source
11	16
17	19
32	27
45	34

interrupt, as well as a growth interrupt when changing the substrate temperature, was performed for all the growths. This mode of growth was utilized to prevent chemical intermixing between the $Sc_xAl_{1-x}N$ and GaN layers. For SIMS studies, 4X repeats of $Sc_xAl_{1-x}N$/GaN layers of ~60 nm/60 nm thicknesses were grown on a ~270 nm GaN buffer layer on a semi-insulating GaN-Al_2O_3 substrate. One multilayer heterostructure consisting of four $Sc_xAl_{1-x}N$ layers was grown for each Sc source, resulting in two samples for comparative SIMS studies. For electrical measurements, ~100 nm thick $Sc_xAl_{1-x}N$ layers were grown on a ~200 nm epitaxial n^+GaN layer of Si doping $N_D \sim 10^{19}$ cm^{-3}. The Sc content was varied across four samples with each Sc source, giving a total of eight samples for vertical electrical conductivity studies.

Table I summarizes the Sc contents obtained via RBS measurements between the two 4× period $Sc_xAl_{1-x}N$-GaN heterostructures. The surface crystalline structure during the growth was tracked by *in situ* RHEED. Figure 1 shows the evolution of RHEED images during the growth of the 4-period $Sc_xAl_{1-x}N$/GaN multilayer heterostructures. The RHEED images viewed along the $\langle 11\bar{2}0 \rangle$ azimuth suggest that all layers are single-crystalline and epitaxial. Bisecting Kikuchi lines are seen for the x = 0.16 $Sc_xAl_{1-x}N$ layer indicating high crystal quality and coherence. This is expected since $Sc_{0.16}Al_{0.84}N$ is close to the nominally lattice-matched Sc composition (x = 0.18) with GaN. As the Sc content is increased or as the Sc content deviates significantly from ~18%, spots develop on the primary 1 × 1 streak patterns, and the streaks become more diffuse. This is indicative of decreasing crystalline quality and agrees with an increased in-plane lattice mismatch with GaN. Despite this trend, all the subsequently grown GaN layers retained their primary streak patterns. This suggests that GaN maintained a wurtzite crystal structure, and the underlying $Sc_xAl_{1-x}N$ is predominantly wurtzite. Any underlying defects do not disturb the epitaxy enough to prevent the formation of the thermodynamically stable wurtzite phase in GaN. AFM images (not shown) acquired after growth of both samples showed small hillocks on the surface with an rms roughness of ~2 nm related to the characteristic of the dislocation-mediated surface morphology of MBE-grown GaN. No significant difference was observed for the two samples in the AFM images.

Figure 2 shows, in a comparative fashion, the x-ray diffraction patterns measured for the two $Sc_xAl_{1-x}N$/GaN heterostructures grown with the two Sc sources. The substrate sapphire and the thick GaN peaks are at the same angle. The symmetric geometry 2θ-ω scans showed crystalline behavior in both samples, with $Sc_xAl_{1-x}N$ 0002 peaks appearing near 36° 2θ for the lowest Sc content layer and increasing to higher angles (smaller c-axis lattice parameter) for the layers with higher Sc contents. The Sc contents in these two samples were measured by RBS. The sample grown with the

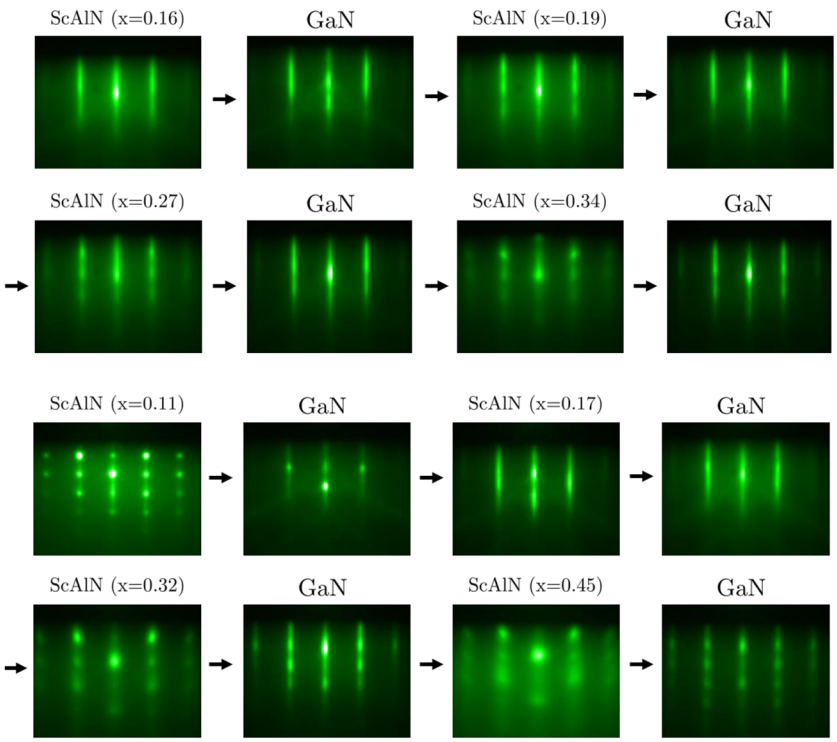

FIG. 1. Evolution of the RHEED pattern along the ⟨110⟩ zone axis for both 4× period $Sc_xAl_{1-x}N$/GaN multilayer heterostructures with an increasing Sc composition in respective layers during the growth with x = 0.16–0.34 and x = 0.11–0.45 for the higher and lower purity Sc sources, respectively. The arrows indicate the time sequence after the growth of each layer. All diffraction images suggest that the layers are epitaxial and single-crystalline except for the x = 0.45 layer. The structural degradation of the highest Sc content $Sc_xAl_{1-x}N$ layer is indicated by the spotty pattern: Nevertheless, the diffraction pattern suggests it to be crystalline. The GaN layers recover their 1 × 1 streaks overall and maintain their hexagonal crystal structure.

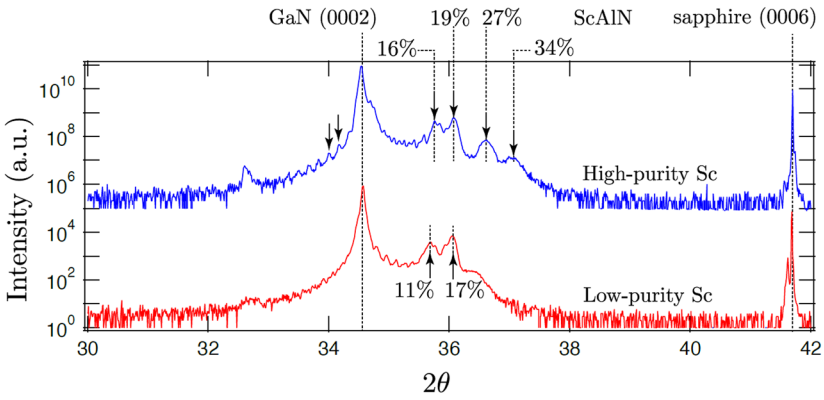

FIG. 2. Symmetric 2Θ-ω XRD scans, showing $Sc_xAl_{1-x}N$ wurtzite 0002 peaks for lower Sc contents in both samples and the Al_2O_3 0006 peak from the substrate. The sample grown with a higher purity Sc source shows XRD peaks near the expected positions for Sc compositions of x = 0.27 and 0.34, indicating higher crystallinity.

higher purity Sc source has respective layer Sc contents of 16, 19, 27, and 34 at. %, respectively (x = 0.16, 0.19, 0.27, and 0.34). These Sc contents correspond to the out of plane lattice parameters of 5.01, 4.98, 4.91, and 4.85 Å, respectively. The sample grown with the lower purity Sc source has XRD peaks for 11 and 17 at. % Sc (x = 0.11 and 0.17). These correspond to the out of plane lattice parameters of 5.03 and 4.99 Å, respectively This is in agreement with a trend of a slight increase in the out of plane lattice parameter relative to AlN and then a decrease in the out of plane lattice parameter, as the Sc content is increased past ~17% (x = 0.17). This non-monotonic change and deviation from Vegard's law has been predicted by recent theoretical calculations. This likely originates from a competition between increasing average bond length and increased tetrahedral structural distortion, which tilts the tetrahedral bonds away from the c-axis.[53,54] It is noted that the measured out of plane lattice parameters for MBE grown $Sc_xAl_{1-x}N$ can vary depending on the relative growth conditions (e.g., III/V ratio and substrate temperature).

A difference is found in the XRD of Fig. 2 for the two samples with different Sc purity sources. The XRD peaks indicated by downward arrows in the higher purity Sc source sample that correspond to the two highest Sc contents (x = 0.27 and 0.34) are absent in the lower Sc purity sample. Despite the Sc contents being different between the two samples overall, an XRD peak for the x = 0.32 layer in the lower purity Sc sample would still be expected as a peak is seen for the x = 0.34 layer in the higher purity Sc sample. In addition, the interference fringes to the left of the main GaN 0002 peak are more prominent in the higher-purity Sc source sample, indicating superior $Sc_xAl_{1-x}N$-GaN interfaces. The peak near 32.6° 2θ found in the higher purity Sc source sample likely corresponds to the $10\bar{1}0$ orientation of hexagonal $Sc_xAl_{1-x}N$, though its origin is currently unclear.

In general, the comparison of the x-ray spectra indicates a superior crystalline quality for high Sc compositions (near x = 0.34) for the sample grown with the higher purity Sc source. Chemical differences between sources are not expected to cause significant structural differences. The exact reason for this structural difference is currently unclear and may result from a difference in Sc contents. It is noted that the Sc contents are different between samples due to deviations in the Sc flux from the electron beam evaporation between two samples. One possibility relating structural differences between samples to chemical differences is that the significantly higher levels of dopant-level impurities in the lower purity Sc source affect the nucleation and growth of the respective $Sc_xAl_{1-x}N$ layers, which generate more extended defects. This is discussed further after the structural and chemical analyses of these multilayer heterostructures.

Figure 3 compares wide field-of-view and atomic-resolution HAADF-STEM images of the $Sc_xAl_{1-x}N$/GaN heterostructures each grown with different Sc source purities. The wider-view images were taken using a longer camera length (CL) of 245 mm to better assess extended defects and strain. An increased defect density, including threading dislocations in $Sc_xAl_{1-x}N$ layers, is vividly seen in both samples as the Sc content is increased (x = 0.32 and 0.45). It can be found qualitatively that at layers with higher Sc contents, the sample grown with the lower purity Sc source has an increased density of extended defects relative to the sample grown with the higher purity Sc source. Atomic resolution images were taken using a shorter CL of 160 mm for atomic number (Z)-contrast dominant imaging. Because Ga has a larger atomic number than Sc and Al, GaN appears brighter than $Sc_xAl_{1-x}N$. The images reveal relatively abrupt interfaces between the $Sc_xAl_{1-x}N$ and GaN layers. In addition, all GaN layers are found to adopt the wurtzite crystal structure and maintain a metal-polar orientation throughout the heterostructure layers.

Visually, one could interpret the lower Sc content layers (x = 0.11 and 0.17) to be of higher quality in the sample grown with the lower purity Sc source. However, due to FIB milling, the final sample thicknesses along the electron beam direction are different: 83 and 157 nm for samples grown with lower and higher purity sources, respectively. The method for determining the sample thicknesses is discussed in the supplementary material. A comparison of the dislocation density for the $Sc_xAl_{1-x}N$ (x = 0.17) layer from the heterostructure with the lower purity Sc source with $Sc_xAl_{1-x}N$ (x = 0.16) in the heterostructure with the higher purity Sc source was performed. The dislocation density of the latter (4.85×10^{10} cm^{-2}) is ~1.5 times lower than the former (7.35×10^{10} cm^{-2}), indicating that the $Sc_xAl_{1-x}N$ layers grown with the higher purity Sc source are, indeed, of high quality.

Figure 4 shows the SIMS measurement of the chemical concentrations of desired and undesired elements as a function of depth from the surface for the two samples with different Sc purities. Figure 4(a) shows the atomic concentrations of Sc, Al, and Ga in the multilayer region indicating the uniformity of the Sc content in

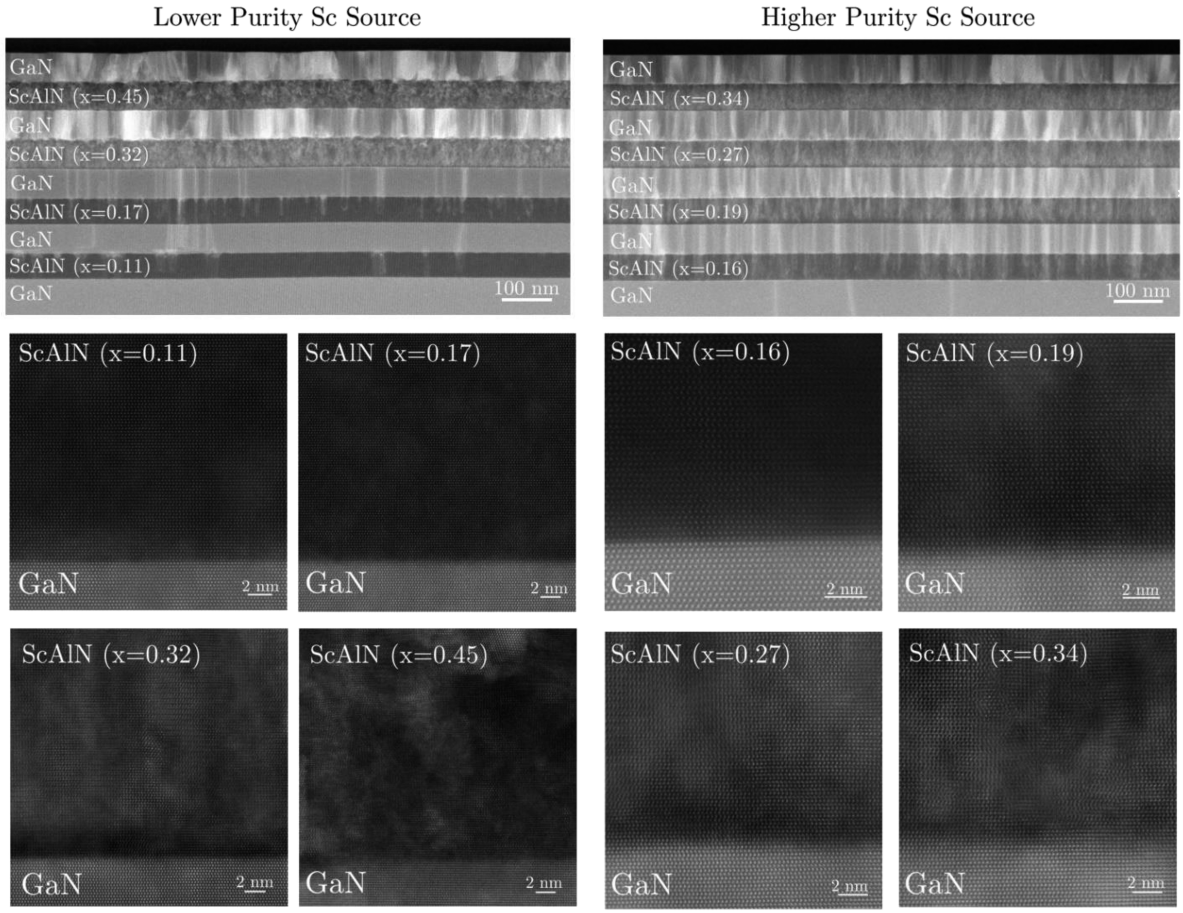

FIG. 3. STEM images of heterostructures grown with a lower purity Sc source (left) and higher purity Sc source (right). Wide field-of-view heterostructure images are taken with a longer camera length (CL) of CL = 245 mm to show contrast from extended defects and strain. Increased defect densities are seen in the high composition $Sc_xAl_{1-x}N$ layers. Atomic resolution images near the interfaces are taken with a shorter CL = 160 mm to highlight atomic number contrast and chemical abruptness of the interfaces. These also show GaN is wurtzite in every layer.

the $Sc_xAl_{1-x}N$ layers for the higher Sc purity multilayer. The measurement of the atomic Al, Sc, and Ga concentrations of the lower Sc purity multilayer is very similar to Fig. 4(a) and, therefore, not shown. Figures 4(b)–4(c) indicate the significant difference in the unintentional impurity levels incorporated in the $Sc_xAl_{1-x}N$ layers in the two films. The heterostructure grown with a higher purity Sc source has 1–3 orders of magnitude lower levels of C, O, and F impurities. The data for the layer with the highest Sc content in each sample, x = 0.34 in the higher purity Sc sample and x = 0.45 in the lower purity Sc sample, show that peak oxygen levels are reduced from ~1×10^{19} to 5×10^{17} cm^{-3}, peak carbon levels are reduced from ~6×10^{18} to ~1×10^{17} cm^{-3}, and peak fluorine levels are reduced from ~8×10^{18} to 2×10^{15} cm^{-3}. Integrating the impurity concentration curves gives C, O, and F densities of 9.4×10^{11}, 3.9×10^{12}, and 1.2×10^{10} atoms/cm^2, respectively, at the x = 0.34 layer in the higher purity Sc sample. For the x = 0.45 layer in the lower purity Sc sample, the C, O, and F densities are 3.21×10^{13}, 8.32×10^{13}, and 1.0×10^{13} atoms/cm^2, respectively. The fluorine concentration may not be physical in the sample grown with the higher purity Sc source as it is extremely close to the detection limit in AlN and it is unknown if the detection limit changes for $Sc_xAl_{1-x}N$.

Overall, the data directly indicate that impurities from the Sc source are incorporated in the resultant epitaxial $Sc_xAl_{1-x}N$ layers although the background partial pressures of fluorine, oxygen, and carbon levels are below the residual gas analyzer detection limit of ~10^{-12} Torr in the MBE growth chamber. Since the oxygen level in the higher purity Sc source is ~200 ppm, it suffices to state that some of the oxygen in the Sc source also ends up in the MBE $Sc_xAl_{1-x}N$ layers. This agrees with the refractory nature of Sc_2O_3 and the difficulty in the removal of oxygen from Sc. Nevertheless, the trends between samples indicate utilizing a higher purity Sc source is a promising way to reduce impurity levels in $Sc_xAl_{1-x}N$ and is an important step toward revealing the intrinsic properties of this material. Meanwhile, point defects arising from oxygen substitution on a nitrogen site in traditional III-nitride semiconductors (e.g., GaN, AlN, InN, and their alloys) act as electron donors.[55] Given

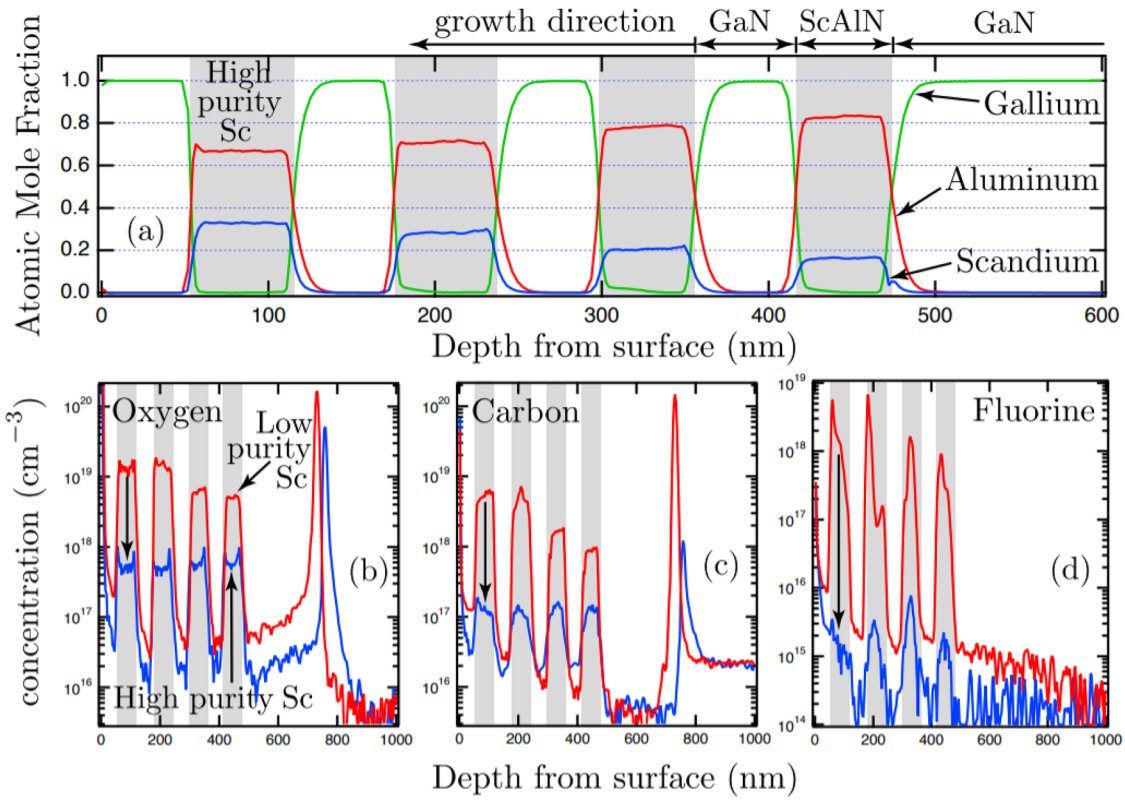

FIG. 4. RBS and SIMS measurements of the chemical composition profiles in the $Sc_xAl_{1-x}N$/GaN heterostructures. (a) The change in atomic mole fractions of Sc, Al, and Ga in the higher purity Sc heterostructure. The three add to a stoichiometric composition throughout from the surface to nucleation interface, which is ~700 to 800 nm below the surface as visible in (b) and (c) as the oxygen and carbon peaks. For the higher purity Sc source, the Sc contents in the $Sc_xAl_{1-x}N$ layers have higher uniformity. The heterostructure grown with the lower purity Sc source shows orders of magnitude higher levels of carbon, oxygen, and fluorine as seen in (b)–(d), which originate from the Sc source material itself.

chemical trends and predicted behavior in GaN, AlN, and ScN, as well as experimental data for ScN, fluorine substitution on a nitrogen site is expected to act as an electron donor.[56–60] Therefore, controlling their levels in the III-nitride films is critical toward achieving high resistivity layers that can sustain large electric fields without conduction losses. This will be possible by reducing the unintentional *n*-type carrier density and moving the Fermi level deeper into the energy bandgap of $Sc_xAl_{1-x}N$.

To investigate the consequence of the chemical differences between the two Sc sources on the electronic properties of $Sc_xAl_{1-x}N$, eight samples of single layer $Sc_xAl_{1-x}N/n^+GaN$ heterostructures were grown on n^+GaN bulk substrates. Four samples utilized the higher purity Sc source and four samples utilized the lower purity Sc source. The thickness of the $Sc_xAl_{1-x}N$ layers was ~100 nm for all samples, which was grown by MBE on ~200 nm Si-doped n^+GaN layer as shown in Fig. 5(a). These samples were grown at the same substrate temperature and III/V ratio as the heterostructures mentioned earlier in the manuscript. The Sc content was varied for the four samples. H1–H4 refer to the lowest to highest Sc contents measured for the higher purity Sc samples: 16, 19, 27, and 34 at. %, respectively. The Sc contents measured for the lower purity Sc samples are 16, 23, and 31 at. %, respectively. The last sample likely had higher Sc contents that were not traceable via XRD due to a destabilization of the wurtzite phase and c-axis orientation. The Sc content was assigned based on the XRD peak angles for the $Sc_xAl_{1-x}N$ 0002 peaks in the samples (not shown) and compared to the 0002 peak positions in the prior $Sc_xAl_{1-x}N$-GaN samples in this report calibrated with RBS data to evaluate the Sc content. The $Sc_xAl_{1-x}N$ 0002 XRD full-width-half-maximum (FWHM) values are 0.02°–0.05° for samples H1–H4 and 0.06°–0.10° for the lower purity Sc samples. Indium was mounted on the backside of the n^+GaN substrate as bottom electrodes, and top electrodes were lithographically patterned 40 × 40 μm^2 Ti/Au metal stacks.

The comparative current vs voltage characteristics shown in Figs. 5(b) and 5(c) illustrate a rather severe effect of the Sc source purity on electrical leakage through the $Sc_xAl_{1-x}N$ films for biases ranging from −20 to +20 V. To obtain a very crude estimate, neglecting internal fields and depletion regions in the n^+GaN, this would correspond to an effective electric field of −2 to +2 MV/cm in the $Sc_xAl_{1-x}N$ layer. While this field can lead to Fowler–Nordheim tunneling, it is far below the expected electrical breakdown field of GaN (~3.5 MV/cm). The breakdown fields of sputter deposited $Sc_xAl_{1-x}N$

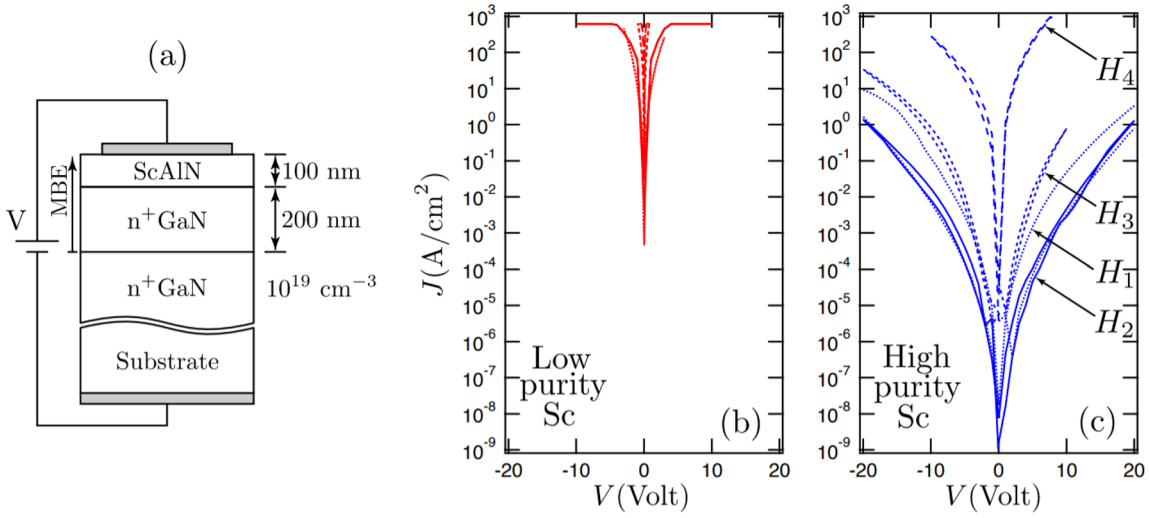

FIG. 5. Electrical properties of $Sc_xAl_{1-x}N/n^+GaN$ heterostructures via quasi-static I–V measurements at room temperature. Schematic of the heterostructure is shown on the left (a). Electrical current density comparison of $Sc_xAl_{1-x}N$ (b)–(c), with samples grown with a lower and higher purity Sc source. Here, the electrical current density is reported as the measurement current divided by the area of the Ti/Au electrode. The electrical current density is significantly reduced in the samples grown with a higher purity Sc source.

are generally larger than 3.4 MV/cm[61] and above, so the insulating characteristics of MBE grown $Sc_xAl_{1-x}N$ can be improved further.

The $Sc_xAl_{1-x}N$/GaN heterostructures grown with the lower purity Sc source shown in Fig. 5(b) are found to be highly leaky. The lower purity Sc source, therefore, is not desirable for the growth of $Sc_xAl_{1-x}N$ layers targeted for electrical heterostructure barriers. This high conductivity can be due to several reasons, ranging from the high density of oxygen and fluorine impurities at low Sc compositions visible in the SIMS measurements to structural defects at high compositions that are evident in the x-ray and TEM images, increasing material conductivity and electrical leakage.

Comparing the current densities at 5 V (~0.5 MV/cm electric field) bias between both sets of samples leads to the higher-purity Sc samples shown in Fig. 5(c) in blue having ~5 to 7 orders of magnitude lower values at all Sc contents other than the highest studied (x ~ 0.33). No significant rectification effect is observed in any of the structures. The current density reaches ~1 mA/cm^2 at ~1 MV/cm for the lowest Sc content heterostructure. The current density increases with the Sc content, which is attributed to the combined effects of smaller bandgap and band offsets, as well as increasing defect-assisted leakage currents from increased structural distortion. The measured current densities are higher than those predicted by thermionic emission and Fowler–Nordheim tunneling, suggesting defect-assisted leakage currents. The $Sc_xAl_{1-x}N$ 0002 XRD FWHM values between two sets of samples are different, but the relatively small difference alone would not be expected to result in a large leakage current difference. For low Sc contents, the $Sc_xAl_{1-x}N$ layers do act as an effective barrier, though its insulating properties can be improved further. Some amount of hysteresis is observed in the I–V measurements, suggesting the presence of trap states in this heterostructure. While the lowered currents suffice for certain passive uses of $Sc_xAl_{1-x}N$, reducing electrical leakage in epitaxial $Sc_xAl_{1-x}N$ layers is critical to realize ferroelectric and enhanced piezoelectric behavior. Specifically, large ferroelectric coercive fields on the order of 5 MV/cm (e.g., ~50 V over a 100 nm film) for $Sc_xAl_{1-x}N$ necessitate sustained large electric fields inside the film. Thus, future work in growth must, therefore, find ways to lower the impurities in the Sc source even further to approach such field strengths.

In conclusion, important insights into the structural, chemical, and electrical trends of epitaxially grown $Sc_xAl_{1-x}N$/GaN heterostructures and their dependence on the starting Sc source material are achieved in this work. STEM imaging shows that the epitaxial thin films grown with higher purity Sc show decreased defect densities at high Sc contents relative to the films grown with a lower Sc purity source. This is corroborated in the XRD data where wurtzite peaks at higher Sc contents are absent in the film grown with a lower purity Sc source. SIMS measurements show a 2–4 orders of magnitude reduction of carbon, oxygen, and fluorine impurities for the $Sc_xAl_{1-x}N$ sample grown with a higher purity source. The structural and chemical differences correlate with a significantly (five to seven orders of magnitude) lower electrical leakage in films grown with the higher purity Sc source. This combination of results indicates the significant and beneficial impact a higher purity Sc source has on the combined structural, chemical, and electronic properties of $Sc_xAl_{1-x}N$, and its potential integration with GaN and AlN in the future.

See the supplementary material for convergent beam electron diffraction data and information regarding the thickness evaluation of the $Sc_xAl_{1-x}N$-GaN multilayer heterostructure samples along the beam direction.

This work was supported by the DARPA Tunable Ferroelectric Nitrides (TUFEN) program monitored by Dr. Ronald G. Polcawich. This work was also supported, in part, by NSF DMREF Grant No. 1534303, Cornell's nanoscale facility (Grant No.

NCCI-1542081), AFOSR Grant No. FA9550-20-1-0148, NSF Grant No. DMR-1710298, and the Cornell Center for Materials Research Shared Facilities, which are supported through the NSF MRSEC program (Grant No. DMR-1719875). This work made use of a Helios FIB supported by the NSF (Grant No. DMR-1539918) and a FEI Titan Themis, which was acquired through Grant No. NSF-MRI-1429155, with additional support from Cornell University, the Weill Institute, and the Kavli Institute at Cornell. The authors would also like to acknowledge the Materials Preparation Center, Ames Laboratory, U.S. DOE Basic Energy Sciences, Ames, IA, USA, for supplying the Sc source material. The authors would like to thank Yu-Tsun Shao for the CBED measurements and analysis of the heterostructures. In addition, the authors thank Christian Borglum, Daniel Tseng, Bruce Rothman, Ozgur Celik, and Miki Nakayama at EAG for the SIMS and RBS measurements, data processing, and discussions.

DATA AVAILABILITY

The data that support the findings of this study are available from the corresponding author upon reasonable request.

REFERENCES

[1] S. Fichtner, N. Wolff, F. Lofink, L. Kienle, and B. Wagner, J. Appl. Phys. **125**, 114103 (2019).
[2] S. Bette, S. Fichtner, S. Bröker, L. Nielen, T. Schmitz-Kempen, B. Wagner, C. Van Buggenhout, S. Tiedke, and S. Tappertzhofen, Thin Solid Films **692**, 137623 (2019).
[3] N. Kurz, Y. Lu, L. Kirste, M. Reusch, A. Žukauskaitė, V. Lebedev, and O. Ambacher, Phys. Status Solidi A **215**, 1700831 (2018).
[4] M. A. Caro, S. Zhang, T. Riekkinen, M. Ylilammi, M. A. Moram, O. Lopez-Acevedo, J. Molarius, and T. Laurila, J. Phys.: Condens. Matter **27**, 245901 (2015).
[5] M. Akiyama, T. Kamohara, K. Kano, A. Teshigahara, Y. Takeuchi, and N. Kawahara, Adv. Mater. **21**, 593 (2009).
[6] M. Akiyama, K. Kano, and A. Teshigahara, Appl. Phys. Lett. **95**, 162107 (2009).
[7] Y. Lu, M. Reusch, N. Kurz, A. Ding, T. Christoph, M. Prescher, L. Kirste, O. Ambacher, and A. Žukauskaitė, APL Mater. **6**, 076105 (2018).
[8] K. R. Talley, S. L. Millican, J. Mangum, S. Siol, C. B. Musgrave, B. Gorman, A. M. Holder, A. Zakutayev, and G. L. Brennecka, Phys. Rev. Mater. **2**, 063802 (2018).
[9] M. A. Moram and S. Zhang, J. Mater. Chem. A **2**, 6042 (2014).
[10] S. Zhang, D. Holec, W. Y. Fu, C. J. Humphreys, and M. A. Moram, J. Appl. Phys. **114**, 133510 (2013).
[11] D. Jena, R. Page, J. Casamento, P. Dang, J. Singhal, Z. Zhang, J. Wright, G. Khalsa, Y. Cho, and H. G. Xing, Jpn. J. Appl. Phys., Part 1 **58**, SC0801 (2019).
[12] M.-A. Dubois, P. Muralt, and V. Plessky, in *1999 IEEE Ultrasonic Symposium. Proceedings. International Symposium (Cat No. 99CH37027)* (IEEE, Caesars Tahoe, NV, 1999), pp. 907–910.
[13] M. D. Hodge, R. Vetury, S. R. Gibb, M. Winters, P. Patel, M. A. McLain, Y. Shen, D. H. Kim, J. Jech, K. Fallon, R. Houlden, D. M. Aichele, and J. B. Shealy, in *2017 IEEE International Electron Devices Meeting (IEDM)* (IEEE, San Francisco, CA, 2017), pp. 25.6.1–25.6.4.
[14] A. Hickman, R. Chaudhuri, S. J. Bader, K. Nomoto, K. Lee, H. G. Xing, and D. Jena, IEEE Electron Device Lett. **40**, 1293 (2019).
[15] S. M. Islam, K. Lee, J. Verma, V. Protasenko, S. Rouvimov, S. Bharadwaj, H. (Grace) Xing, and D. Jena, Appl. Phys. Lett. **110**, 041108 (2017).
[16] Z. Zhang, M. Kushimoto, T. Sakai, N. Sugiyama, L. J. Schowalter, C. Sasaoka, and H. Amano, Appl. Phys. Express **12**, 124003 (2019).
[17] N. Takeuchi, Phys. Rev. B **65**, 045204 (2002).
[18] N. Farrer and L. Bellaiche, Phys. Rev. B **66**, 201203 (2003).
[19] J. Casamento, J. Wright, R. Chaudhuri, H. (Grace) Xing, and D. Jena, Appl. Phys. Lett. **115**, 172101 (2019).
[20] A. M. Poston, A. D. Mah, A. R. Taylor, C. Zahn, D. Bienstock, D. F. Smith, F. Wideman, H. F. Yancey, J. M. Riley, and L. Obert, *Heats and Free Energies of Formation of Gallium Sesquioxide and Scandium Sesquioxide* (U.S. Department of the Interior, Bureau of Mines, 1962).
[21] J. Casamento, H. G. Xing, and D. Jena, Phys. Status Solidi B **257**, 1900612 (2020).
[22] G. Borzone, R. Raggio, and R. Ferro, Phys. Chem. Chem. Phys. **1**, 1487 (1999).
[23] K. A. Moltved and K. P. Kepp, J. Phys. Chem. C **123**, 18432 (2019).
[24] K. P. Kepp, Inorg. Chem. **55**, 9461 (2016).
[25] M. Li, J. Xie, B. Chen, N. Wang, and Y. Zhu, in *2019 IEEE International Ultrasonics Symposium (IUS)* (IEEE, Glasgow, UK, 2019), pp. 1124–1126.
[26] C. S. Sandu, F. Parsapour, S. Mertin, V. Pashchenko, R. Matloub, T. LaGrange, B. Heinz, and P. Muralt, Phys. Status Solidi A **216**, 1800569 (2019).
[27] Y. Lu, M. Reusch, N. Kurz, A. Ding, T. Christoph, L. Kirste, V. Lebedev, and A. Žukauskaitė, Phys. Status Solidi A **215**, 1700559 (2018).
[28] P. M. Mayrhofer, P. O. Å. Persson, A. Bittner, and U. Schmid, Microsyst. Technol. **22**, 1679 (2016).
[29] A. Zukauskaite, G. Wingqvist, J. Palisaitis, J. Jensen, P. O. Å. Persson, R. Matloub, P. Muralt, Y. Kim, J. Birch, and L. Hultman, J. Appl. Phys. **111**, 093527 (2012).
[30] F. Parsapour, V. Pashchenko, S. Mertin, C. Sandu, N. Kurz, P. Nicolay, and P. Muralt, in *2017 IEEE International Ultrasonics Symposium (IUS)* (IEEE, Washington, DC, 2017), pp. 1–4.
[31] S. Mertin, V. Pashchenko, F. Parsapour, C. Nyffeler, C. S. Sandu, B. Heinz, O. Rattunde, G. Christman, M.-A. Dubois, and P. Muralt, in *IEEE International Ultrasonics Symposium (IUS)* (IEEE, Washington, DC, USA, 2017), pp. 1–4.
[32] O. Zywitzki, T. Modes, S. Barth, H. Bartzsch, and P. Frach, Surf. Coat. Technol. **309**, 417 (2017).
[33] D. Wu, Y. Chen, S. Manna, K. Talley, A. Zakutayev, G. L. Brennecka, C. V. Ciobanu, P. Constantine, and C. E. Packard, IEEE Trans. Ultrason., Ferroelectr., Freq. Control **65**, 2167 (2018).
[34] P. Wang, D. A. Laleyan, A. Pandey, Y. Sun, and Z. Mi, Appl. Phys. Lett. **116**, 151903 (2020).
[35] K. Frei, R. Trejo-Hernández, S. Schütt, L. Kirste, M. Prescher, R. Aidam, S. Müller, P. Waltereit, O. Ambacher, and M. Fiederle, Jpn. J. Appl. Phys., Part 1 **58**, SC1045 (2019).
[36] M. T. Hardy, B. P. Downey, N. Nepal, D. F. Storm, D. S. Katzer, and D. J. Meyer, Appl. Phys. Lett. **110**, 162104 (2017).
[37] R. Dargis, A. Clark, A. Ansari, Z. Hao, M. Park, D. Kim, R. Yanka, R. Hammond, M. Debnath, and R. Pelzel, Phys. Status Solidi A **217**, 1900813 (2020).
[38] T. E. Kazior, E. M. Chumbes, B. Schultz, J. Logan, D. J. Meyer, and M. T. Hardy, in *2019 IEEE MTT S International Microwave Symposium (IMS)* (IEEE, Boston, MA, 2019), pp. 1136–1139.
[39] A. J. Green, J. K. Gillespie, R. C. Fitch, D. E. Walker, M. Lindquist, A. Crespo, D. Brooks, E. Beam, A. Xie, V. Kumar, J. Jimenez, C. Lee, Y. Cao, K. D. Chabak, and G. H. Jessen, IEEE Electron Device Lett. **40**, 1056 (2019).
[40] M. Park, Z. Hao, D. G. Kim, A. Clark, R. Dargis, and A. Ansari, in *2019 20th International Conference on Solid-State Sensors, Actuators Microsystems and Eurosensors XXXIII (Transducers Eurosensors XXXIII)* (IEEE, Berlin, Germany, 2019), pp. 450–453.
[41] A. Ansari, in *2019 IEEE MTT-S International Wireless Symposium (IWS)* (IEEE, Guangzhou, China, 2019), pp. 1–3.
[42] J. Ligl, S. Leone, C. Manz, L. Kirste, P. Doering, T. Fuchs, M. Prescher, and O. Ambacher, J. Appl. Phys. **127**, 195704 (2020).
[43] S. Leone, J. Ligl, C. Manz, L. Kirste, T. Fuchs, H. Menner, M. Prescher, J. Wiegert, A. Žukauskaitė, R. Quay, and O. Ambacher, Phys. Status Solidi RRL **14**, 1900535 (2020).
[44] M. T. Hardy, E. N. Jin, N. Nepal, D. S. Katzer, B. P. Downey, V. J. Gokhale, D. F. Storm, and D. J. Meyer, Appl. Phys. Express **13**, 065509 (2020).
[45] E. N. Jin, M. T. Hardy, A. L. Mock, J. L. Lyons, A. R. Kramer, M. J. Tadjer, N. Nepal, D. S. Katzer, and D. J. Meyer, ACS Appl. Mater. Interfaces **12**, 52192 (2020).
[46] M. Park, Z. Hao, R. Dargis, A. Clark, and A. Ansari, J. Microelectromech. Syst. **29**, 490 (2020).
[47] P. Wang, B. Wang, D. A. Laleyan, A. Pandey, Y. Wu, Y. Sun, X. Liu, Z. Deng, E. Kioupakis, and Z. Mi, Appl. Phys. Lett. **118**, 032102 (2021).

[48] A. L. Mock, A. G. Jacobs, E. N. Jin, M. T. Hardy, and M. J. Tadjer, Appl. Phys. Lett. **117**, 232107 (2020).
[49] C. Manz, S. Leone, L. Kirste, J. Ligl, K. Frei, T. Fuchs, M. Prescher, P. Waltereit, M. A. Verheijen, A. Graff, M. Simon-Najasek, F. Altmann, M. Fiederle, and O. Ambacher, Semicond. Sci. Technol. **36**, 034003 (2021).
[50] *Purification Process and Characterization of Ultra High Purity Metals*, edited by Y. Waseda and M. Isshiki (Springer, Berlin, Heidelberg, 2002).
[51] F. A. Schmidt and O. N. Carlson, J. Less-Common Met. **50**, 237 (1976).
[52] J. Casamento, C. S. Chang, Y.-T. Shao, J. Wright, D. A. Muller, H. (Grace) Xing, and D. Jena, Appl. Phys. Lett. **117**, 112101 (2020).
[53] D. F. Urban, O. Ambacher, and C. Elsässer, Phys. Rev. B **103**, 115204 (2021).
[54] N. Kurz, A. Ding, D. F. Urban, Y. Lu, L. Kirste, N. M. Feil, A. Žukauskaitė, and O. Ambacher, J. Appl. Phys. **126**, 075106 (2019).
[55] C. G. Van de Walle and J. Neugebauer, J. Appl. Phys. **95**, 3851 (2004).
[56] K.-H. Hong, I. Hwang, H. S. Choi, J. Oh, J. Shin, U.-I. Chung, and J. Kim, Phys. Status Solidi RRL **4**, 332 (2010).
[57] J. S. Cetnar, A. N. Reed, S. C. Badescu, S. Vangala, H. A. Smith, and D. C. Look, Appl. Phys. Lett. **113**, 192104 (2018).
[58] R. Deng, B. D. Ozsdolay, P. Y. Zheng, S. V. Khare, and D. Gall, Phys. Rev. B **91**, 045104 (2015).
[59] Y. Kumagai, N. Tsunoda, and F. Oba, Phys. Rev. Appl. **9**, 034019 (2018).
[60] S. Kerdsongpanya, B. Alling, and P. Eklund, Phys. Rev. B **86**, 195140 (2012).
[61] R. Petrich, S. Strehle, M. Hoffmann, J. Muller, H. Bartsch, K. Tonisch, K. Jaekel, S. Barth, H. Bartzsch, D. Glos, A. Delan, and S. Krischok, in *2019 22nd European Microelectronics and Packaging Conference and Exhibition (EMPC)* (IEEE, Pisa, Italy, 2019), pp. 1–5.